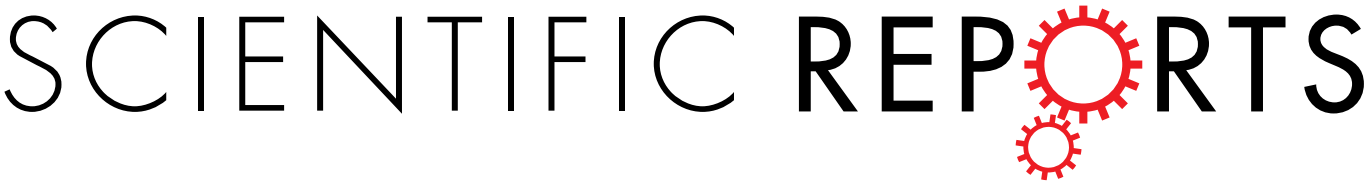

OPEN

Electron tomography and fractal aspects of MoS_2 and MoS_2/Co spheres

Received: 4 May 2017
Accepted: 29 August 2017
Published online: 26 September 2017

Manuel Ramos[2], Félix Galindo-Hernández[1], Ilke Arslan[3], Toby Sanders[3] & José Manuel Domínguez[1]

A study was made by a combination of 3D electron tomography reconstruction methods and N_2 adsorption for determining the fractal dimension for nanometric MoS_2 and MoS_2/Co catalyst particles. *DFT* methods including Neimarke-Kiselev's method allowed to determine the particle porosity and fractal arrays at the atomic scale for the S-Mo-S(Co) 2D- layers that conform the spherically shaped catalyst particles. A structural and textural correlation was sought by further characterization performed by x-ray Rietveld refinement and Radial Distribution Function (RDF) methods, electron density maps, computational density functional theory methods and nitrogen adsorption methods altogether, for studying the structural and textural features of spherical MoS_2 and MoS_2/Co particles. Neimark-Kiselev's equations afforded the evaluation of a pore volume variation from 10 to 110 cm^3/g by cobalt insertion in the MoS_2 crystallographic lattice, which induces the formation of cavities and throats in between of less than 29 nm, with a curvature radius $r_k < 14.4$ nm; typical large needle-like arrays having 20 2D layers units correspond to a model consisting of smooth surfaces within these cavities. Decreasing D_P, D_{Bl}, D_l and D_M values occur when Co atoms are present in the MoS_2 laminates, which promote the formation of smoother edges and denser surfaces that have an influence on the catalytic properties of the S-Mo-S(Co) system.

Catalytic materials are the main pillars of liquid fuels production from hydrocarbons and its role is vital for supplying energy needs from petroleum natural resources. The layered transition metal sulfides (LTMS) such as molybdenum di-sulfide (MoS_2) were used extensively in the petroleum refining industry for more than five decades and these catalysts are referred by the catalysis research community as the "workhorses" of refining processes[1]. From the industrial viewpoint cobalt and nickel are used as promoters of MoS_2 catalytic materials for enhancing deep hydrodesulfurization (HDS)[2–7] for clean fuels production containing ultra-low amounts of sulfur; however, from a basic viewpoint there is no a single model for explaining the promoter effects of Co and Ni. Previous research work by A.L. Farragher and P. Cossee[8] proposed a model that explains the promoter effect of Co and Ni atoms in terms of a "pseudo-intercalation" effect, where Co atoms are located at octahedral sites of MoS_2 layered phase edges, i.e., (1010) type planes; also, B. Delmon *et al.* proposed a model based on the formation of a mix phase of MoS_2 and Co_9S_8, which could be formed by synergic interactions in the unsupported systems[9]; H. Topsøe *et al.* used Mössbauer spectroscopy for demonstrating that chemical bonding occurs at the edge planes of Cobalt-Sulfur-Molybdenum, thus coining the term "CoMoS" phase[10]; also, Chianelli *et al.* proposed a "Rim-Edge" model in an attempt for defining the seat of catalytic activity and specific sites within the MoS_2 stacking structure, which correlates with the activity and selectivity of unsupported systems[11]. More recently, Lauritsen *et al.* reported a combined study using scanning tunneling microscopy (STM) and computer assisted numerical simulations involving plane wave density functional theory methods[12,13], which led them to conclude that metallic states in the cobalt-sulfur bonding play a key role[14]. Furthermore, MoS_2 layered packing structures produce diverse morphologies like nanotubes, needles, fullerenes and spheres, as described by Remškar *et al.*[15], Camacho-Bragado *et al.*[16], Blanco *et al.*[17] and Ramos *et al.*[18]. The latter author used TEM and DFT simulations[19]

[1]Instituto Mexicano del Petróleo (IMP), Eje Central Lázaro Cárdenas Norte 152 Col. San Bartolo Atepehuacan, México, D.F., C.P 07730, USA. [2]Departamento de Física y Matemáticas, UACJ-Instituto de Ingeniería y Tecnología, #450 Avenida del Charro, Cuidad Juárez, 32310, México, USA. [3]Fundamental and Computational Sciences Directorate, Institute for Integrated Catalysis and Environmental Molecular Science Laboratory, Pacific Northwest National Laboratory, Post Office Box 999, Richland, Washington, 99352, United States. Correspondence and requests for materials should be addressed to J.M.D. (email: jmdoming@imp.mx)

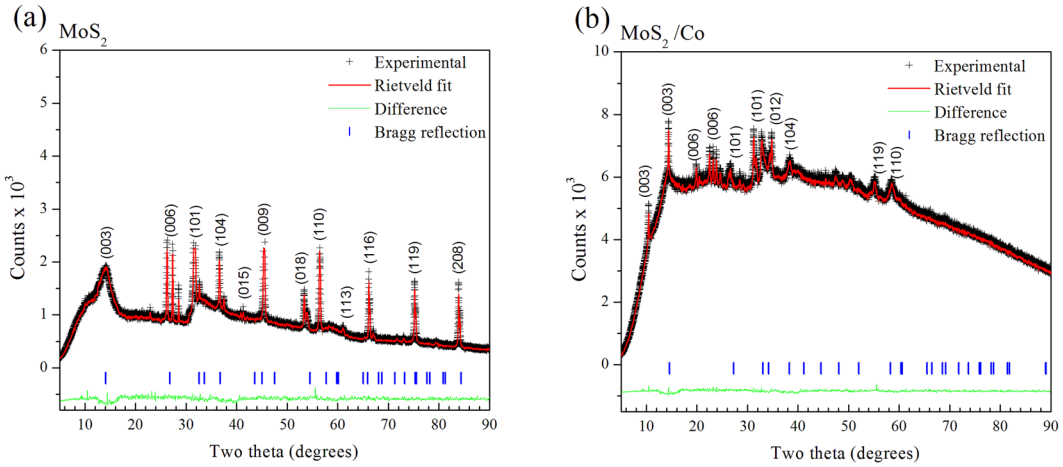

Figure 1. Powder x-ray diffraction patterns and Rietveld refinement for (**a**) MoS_2 and (**b**) Co/MoS_2 samples, it is possible to observe a sharp peak at (003)-basal plane when cobalt atoms are present, compared to pure MoS_2 .

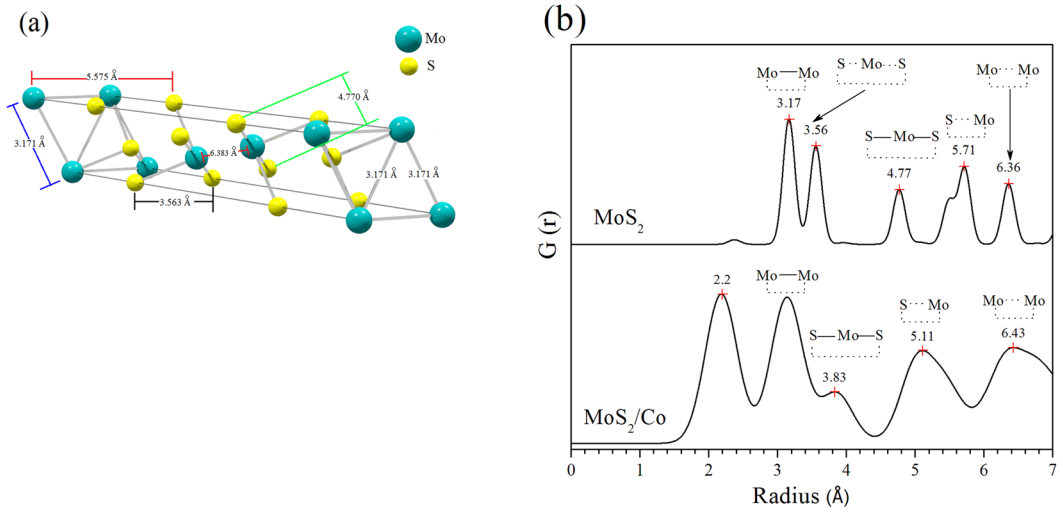

Figure 2. Radial distribution plots for (**a**) MoS_2 crystallographic lattice (a = b = 3.1710 and c = 18.3445 Å) (SG: R3mH). (**b**) Co/MoS_2 it is possible to observe a shifting of Mo-Mo and S-Mo-S peaks, as well the appearance of a new peak at 2.2 Å when cobalt atoms are present in the MoS_2 lattice.

to show that electron donation of cobalt promoters occurs by synergic contact between Co_9S_8 and MoS_2 phases. Furthermore, non-conventional TEM sample holders allowed *in-situ* and *operando* experiments with these phases, as reported by Ramos *et al.*, Helveg *et al.* and Casillas *et al.* These authors showed carburization effects on fresh MoS_2 and MoS_2/Co catalysts[20], crystal formation from molybdenum oxide precursors in the presence of H_2S and H_2 as well as variations of micromechanical properties[21,22]. In other works, STEM 3D tomography was used, as reported by P.A Midgley and R.E. Dunin-Borkowski, to characterize low dimensional materials, proteins and organic specimens[23], while D.A. Muller resolved the atomic structure and chemical bonding of some crystallites[24]. Ziese *et al.* implemented STEM-electron tomography techniques to determine the gold nanoparticles distribution over a SBA-15 type matrix[25], while Arslan *et al.* reported the use of this technique for locating gold particles supported over alumina oxide matrix[26]. The present work afforded a multi-technique analysis of MoS_2 and Cobalt-promoted MoS_2 catalytic particles and a calculation was made of the surface fractal dimension at the molecular level for assessing better the textural and structural features promoted by Co insertion into the MoS_2 lattice. Surface fractal dimensionality is related to the roughness, steps and kinks at the molecular scale and it plays a key role for heterogeneous catalysts, as pointed out by several authors[27–30]. We propose this parameter as an important one for gauging catalytic behavior of Co-promoted-MoS_2 catalysts and as a complement of "electronic effects" induced by insertion of the Co promoter, because it modifies both textural and structural properties of MoS_2; this is the first time that fractal dimensionality is shown as a result of Co-promoter insertion in spherical particles of MoS_2 and the profound effects on both texture and structure as verified in the case of MoS_2/Co system.

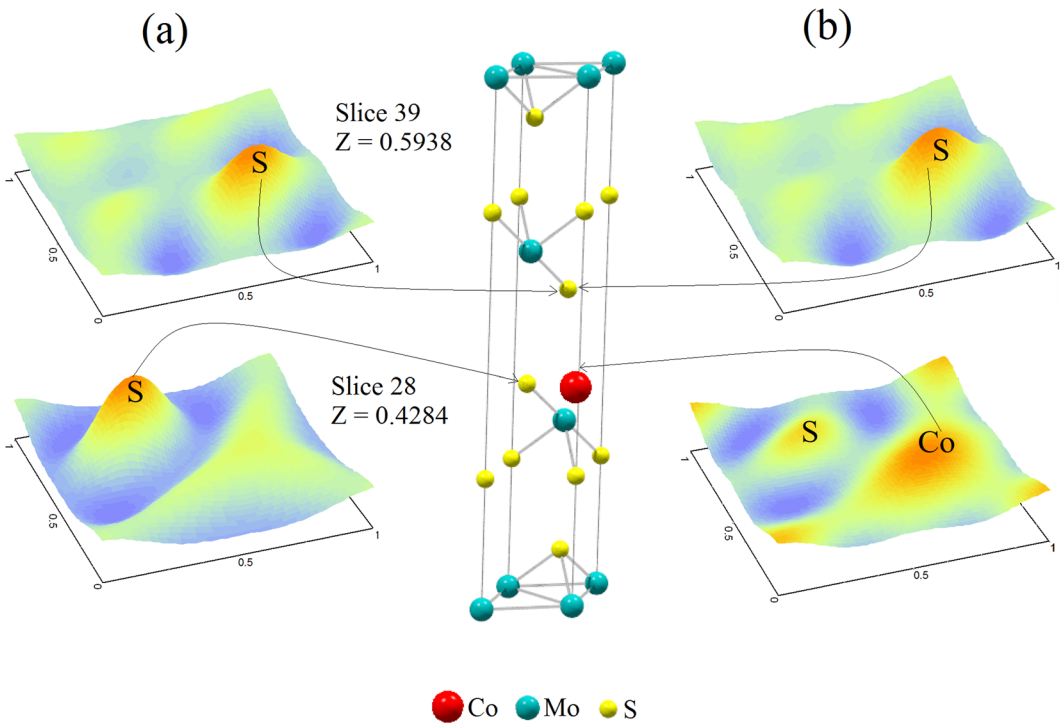

Figure 3. (**a**) Electron density maps to indicate cobalt atoms at the MoS_2 crystallographic lattice and (**b**) for Cobalt atoms into the MoS_2 lattice. (Data calculated using information from powder X-ray diffraction and DFT numerical simulations).

MoS_2 R 3 m H (160)			Lattice: Rhombohedral			
			Atomic fractional coordinates			
Atom	**Type**	**Site**	**x**	**y**	**z**	**Occupancy**
Mo (1)	Mo^{4+}	3a	0.0000	0.0000	1.0000	0.16667
S (1)	S^{2-}	3a	0.0000	0.0000	0.2500	0.16667
S (2)	S^{2-}	3a	0.0000	0.0000	0.7500	0.16667
Lattice parameters (Å)			**Angles**			
a	b	c	α	β	γ	Density (g cm^{-3})
3.1710	3.1710	18.3445	90°	90°	120°	4.992

Table 1. Lattice parameters obtained by Rietveld refinement from x-ray powder diffraction for pure spherical shaped MoS_2 .

Material	Molybdenite crystallite size (nm)	Density (g cm^{-3})	Atomic fractional coordinates of S (2)			
			x	y	z	$O_{S(2)}$
MoS_2	2 (0.4)	4.989	0.0000	0.0000	0.7500	0.16667
MoS_2/Co	8 (0.8)	5.096	0.0000	0.0000	0.8465	0.18400

Table 2. Lattice parameters obtained by Rietveld refinement from x-ray powder diffraction for cobalt promoted MoS_2 . The number in parenthesis corresponds to the standard deviation. $O_{S(2)}$: *S* (2) occupancy (see Table 1).

Results and Discussion

The crystallographic features of hydrothermally as-synthesized Cobalt promoted MoS_2 catalysts were determined by X-ray powder diffraction (Table 1); this comprised the use of Rietveld's refinement method to verify the MoS_2 rhombohedral (R3m) symmetry, in agreement with recent work from Wang *et al.*[31], from which a comparative analysis was performed as shown by Fig. 1, where one observes that a crystallographic variation occurs following cobalt addition during synthesis (Table 2), which can be explained in terms of Frenkel´s point defects[32] (Table 3) caused by interstitial occluded cobalt atoms into the laminar MoS_2 structure, as described by Lauritsen *et al.*[14]. This explains the expansion of about 12.9% (from 0.7500 to 0.8465) of c-axis in the primitive lattice, as demonstrated by Radial Distribution Function results, which indicates interatomic distance variations of 11.7% for

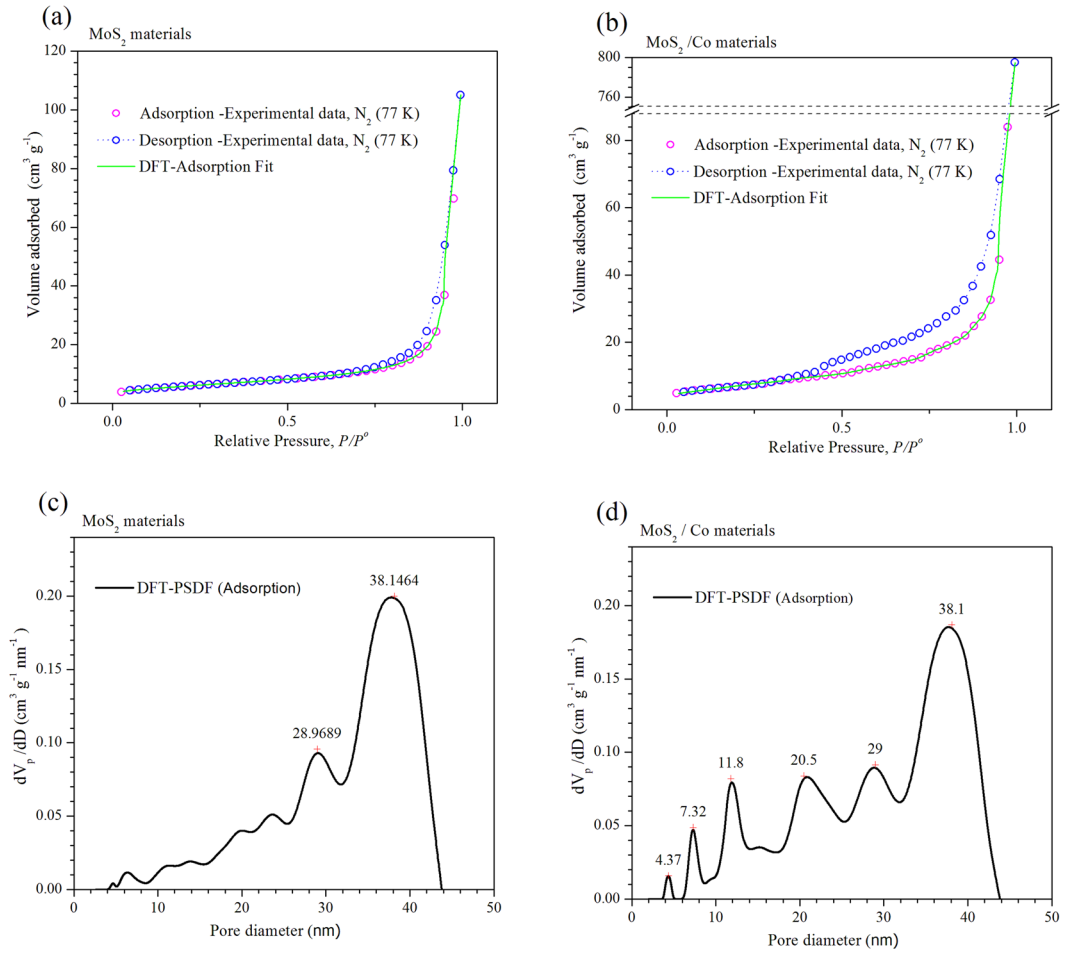

Figure 4. (**a** and **b**) Nitrogen adsorption/desorption isotherms run at 77 K for both cases MoS_2 and Co/MoS_2. (**c** and **d**) Numerical simulation of pore diameter distribution for MoS_2 samples and (**d**) Co/MoS_2 samples.

Material	R_p	R_{wp}	χ^2	R_{exp}
MoS_2	2.95	4.67	2.52	2.94
MoS_2/Co	1.30	1.74	2.07	1.21

Table 3. Statistical parameters after Rietveld refinement for both cases.

	Interatomic distances r (Å)				
Material	Mo—Mo	S····Mo····S	S—Mo—S	S····Mo	Mo····Mo
MoS_2^*	3.171	3.563	4.770	5.575	6.383
$MoS_2^{\#}$	3.170	3.560	4.720	5.710	6.360
MoS_2/Co$^{\#}$	3.140			5.110	6.430

Table 4. Radial distribution function peaks values of MoS_2 and Co/MoS_2 samples. *Theoretical interatomic distances. #Obtained by XRD. —Bond, ----Only distance.

S····Mo and 24.5% for S—Mo—S, with respect to S···Mo···S distance of 3.56 Å (Table 4); these are consistent with displacements of Mo atoms to interstitial sites as confirmed on electron density maps in Figs 2a,b and 3a,b with face *ab* normalized to 1 and with $c = 0.42$ (slice 28) and $c = 0.59$ (slice 39); some specific data are reported in Tables 1-3). In fact, an increase of 10.4% (from 0.16667 to 0.18400) in occupancy position of sulfur $O_{S(2)}$ at the MoS_2/Co lattice implies a stoichiometry variation for MoS_2 to $MoS_{(2+y)}$, thus leading to a molecular increase of crystal density of about 2.14% (from 4.989 to 5.096 g/cm^3) as reported in Table 1); also, the mean crystallites size of MoS_2 vary from 2 nm to 8 nm when cobalt is inserted, as discussed before[18] and indicated in Table 2. The nitrogen adsorption profile of both MoS_2 and MoS_2/Co is consistent with type III isotherms, as shown in Fig. 4a,b with a pore size distribution with maxima at 29 and 38 nm for MoS_2 while these figures vary from 4 nm to 38 nm for

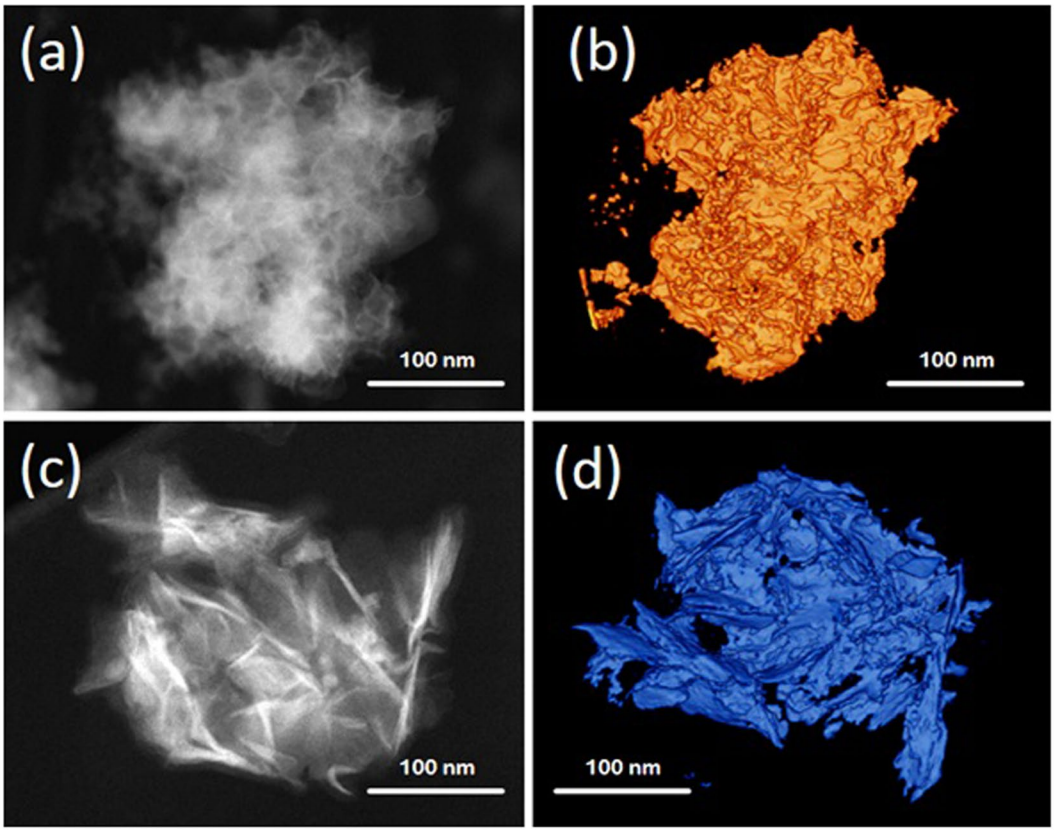

Figure 5. Scanning Transmission Electron Tomography for both MoS_2 and Co/MoS_2 samples. It is possible to determine surface dispersion and change of pore volume when cobalt atoms are present on the sample. Inset: High resolution image of specific section on both cases, one can observe large laminates growth due to addition of cobalt atoms into the MoS_2 lattice.

Material	S^{BET} / S^{DFT} (m^2g^{-1})	V_p ^{DFT} ($mm^3\,g^{-1}$)	Φ ^{DFT} (nm)
MoS_2	20/21	10	29/38
MoS_2/Co	26/27	110	4/7/12/21/29/38

Table 5. Specific surface area, pore volume and mean pore size for both cases. Values were obtained from numerical DFT simulations and experimental isotherms.

Method of analysis	Materials	
	MoS_2	MoS_2/Co
$D_{S\,(Adsorption)}$	2.47 (6.05–40.44)$^{\#}$	2.18 (4.95–20.08)$^{\#}$
$D_{S\,(Desorption)}$	2.52 (6.05–49.40)$^{\#}$	2.25 (6.05–16.44)$^{\#}$

Table 6. Fractal dimension parameters as calculated by Neimark-Kiselev from isotherm curves for MoS_2 and Co/MoS_2 samples. *Ds* scaling interval ∈ [2, 3]; $^{\#}$Radius of curvature (nm).

MoS_2/Co as presented in Fig. 4c,d, thus indicating weak interactions between adsorbate and absorbent; also, a H3 type hysteresis loop (IUPAC standards) is observed in both cases, at the relative pressure (P/P°) interval between 0.4 and 0.45, thus leading to a model akin with slit-shaped pores, which was verified by electron tomography, as presented in Fig. 5a,b, thus indicating a higher N_2 uptake after comparing MoS_2 and MoS_2/Co (i.e., a variation of more than 727%); the adsorption isotherm at $P/P° \sim 0.8$ suggests the formation of condensate at the pores neck for $P/P° > 0.9$, i.e., a liquid–vapor menisci move towards the cavity of the particles, until pores filling with condensates occurs. With the purpose of understanding better this phenomena a series of DFT numerical simulations were completed to determine relevant pore structure parameters (i.e., S^{BET}/S^{DFT}, V_p^{DFT} and Φ^{DFT})as shown in Table 5 ; We propose this parameter as an important one for gauging catalytic behavior of Co-promoted-MoS_2 catalysts and as a complement of "electronic effects" induced by insertion of the Co promoter, because it modifies

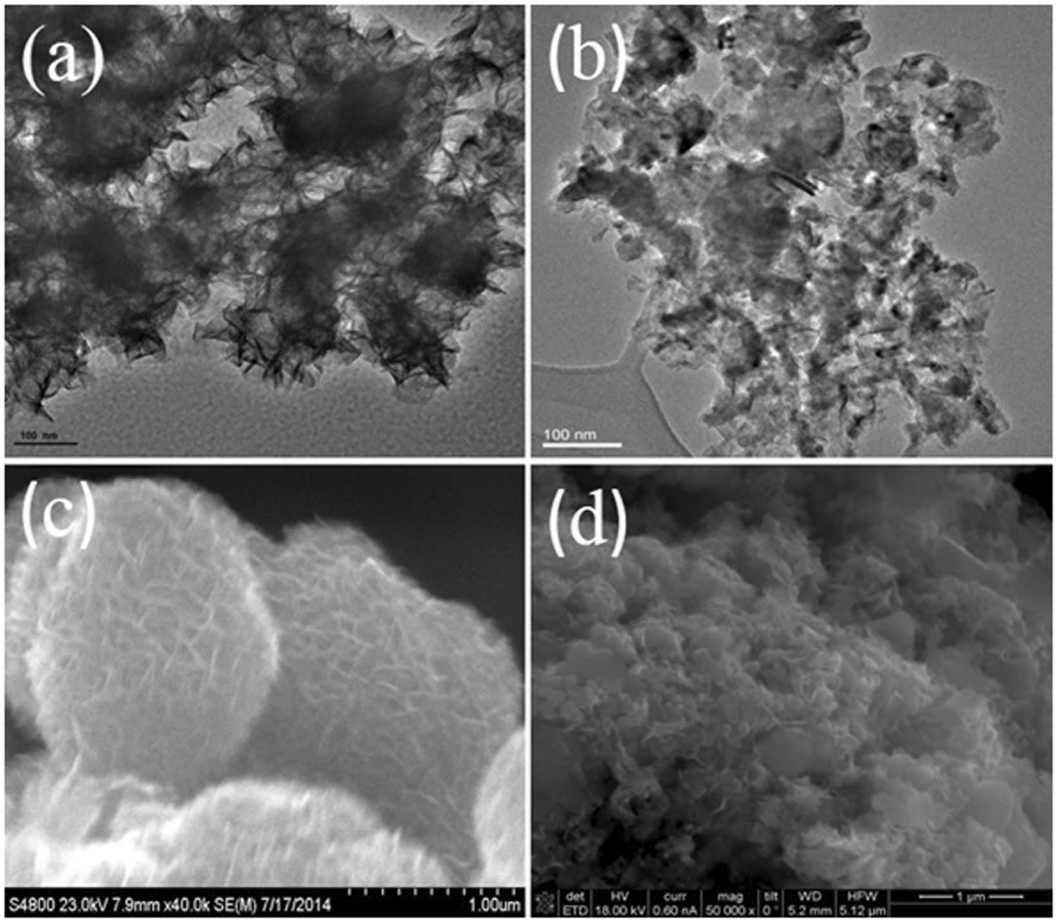

Figure 6. High resolution transmission electron microscopy images: (**a** and **b**) are TEM-images (scale bar 100 nm) corresponding to MoS_2 and Co/MoS_2 respectively. (**c** and **d**) are scanning electron microscopy images (scale bar 1.0 μm) of MoS_2 and Co MoS_2 using both techniques, to determine surface dispersion when cobalt atoms are added, as reported before[18].

Material	Method of analysis				
	D_p	D_B	D_I	D_M	STEM-porosity (%)
MoS_2	1.17 ± 0.01	1.71 ± 0.02	1.83 ± 0.01	1.86 ± 0.01	14.6
MoS_2/Co	1.05 ± 0.01	1.57 ± 0.01	1.64 ± 0.01	2.21 ± 0.01	23.6

Table 7. Fractal dimension parameters and porosity as calculated by different methods from STEM images. D_P, D_B, D_I and D_M are measured from STEM-images; D_p scaling interval ∈ [1, 2]; D_B scaling interval ∈ [1, 2]; D_I scaling interval ∈ [1, 2]; $D_M \geq 1$.

both textural and structural properties of MoS_2; this is the first time that fractal dimensionality is shown as a result of Co-promoter insertion in spherical particles of MoS_2 and the profound effects on both texture and structure as verified in the case of MoS_2/Co system[32]. Thus, a summary of these results is presented in Table 5 where one observes an increase of 29% in S^{BET}/S^{DF}, with a further increase up to 110% for V_p^{DFT} as a result of the overall increase of N_2 uptake upon insertion of cobalt atoms in the MoS_2 lattice. The calculation of Fractal dimension from transmission electron micrographs and the use of Neimark-Kiselev equation in $\boldsymbol{D_{s(adsorption/desorption)}}$ led to determine a decrease of 12% after insertion of cobalt (i.e., details are shown in Tables 6–7), thus implying a lower fractal dimension as exhibited in Fig. 5c,d for r_k values within the interval 6.05–40.44 nm for the MoS_2 spherically shaped particles while r_k values fall within the interval 4.95–20.08 nm for MoS_2/Co system that is spread on the surface, which is observed by STEM tomography (Table 7) as presented in Fig. 6a,b, from which the fractal dimension is obtained using D_P, D_B, D_I and D_M methods, i.e., 1.17 and 1.05 are the fractal dimensions for MoS_2 and MoS_2/Co, while D_B decreases from 1.71 to 1.57due to the surface topology associated with cobalt addition; D_I indicates dispersion of the surface due to the cobalt presence and finally D_M determines a dense surface on MoS_2/Co as observed by larger array of laminates revealed by high-resolution STEM (insets of Fig. 6a,b). Additionally, a second run of fractal calculations were done using TEM-2D images, from which fractal values show a decreasing

Method of analysis	TEM images scale bar at 100 nm	
	MoS_2	MoS_2/Co
D_P	1.67 ± 0.25	1.25 ± 0.24
D_B	1.69 ± 0.08	1.60 ± 0.06
D_I	1.68 ± 0.37	1.40 ± 0.02
D_M	2.00 ± 0.09	2.32 ± 0.17

Table 8. Fractal dimension parameters as calculated by different methods from high-resolution TEM images for MoS_2 and Co/MoS_2. D_P, D_B, D_I and D_M are measured from TEM-images; D_p scaling interval ∈ [1, 2]; D_B scaling interval ∈ [1, 2]; D_I scaling interval ∈ [1, 2]; $D_M \geq 1$.

Method of analysis	SEM-images at 1.0 µm	
	MoS_2	MoS_2/Co
D_p	1.64 ± 0.03	1.07 ± 0.02
D_B	1.90 ± 0.01	1.37 ± 0.01
D_I	1.92 ± 0.01	1.47 ± 0.01
D_M	1.98 ± 0.01	2.02 ± 0.02

Table 9. Fractal dimension parameters as calculated by different methods from SEM images for both MoS_2 and cobalt promoted MoS_2 samples. D_P, D_B, D_I and D_M are measured from TEM-images; D_p scaling interval ∈ [1, 2]; D_B scaling interval ∈ [1, 2]; D_I scaling interval ∈ [1, 2]; $D_M \geq 1$.

trend with the cobalt presence, with values of D_P (25.0%), D_B (5.3%), D_I (17.0%) and D_M (16.0%) as well as when using scanning electron images with values of D_P (34.7%), D_B (28.0%), D_I (23.4%) and D_M (1.9%). See Tables 8–9.

Conclusion

The abovementioned results led us to conclude that chemical state and geometric features together might play an important role, i.e., cobalt atom radius is about 20% larger than sulfur atoms while cobalt ions (Co^{+}) are about 40% the size of sulfur ion S^{2-}; also, the specific hydrothermal synthesis method could contribute too. It was found that Co tends to occupy MoS_2 edges, as determined by Rietveld's refinement method, thus the "CoMoS phase" should be formed. Moreover, the use of Neimark-Kiselev set of equations led us to conclude that cobalt insertion into the MoS_2 crystalline arrays induce a pore volume increase from 10 to 110 cm^3/g, which provokes an increase of the diameter of cavities as well as formation of throats with diameters smaller than 29 nm and $r_k < 14.4$ nm, which explains the higher N_2 consumption during the isotherm runs. Additionally, cobalt insertion promotes formation of large needle-like laminates with a stacking average of ~20 2D layers, as observed by high resolution STEM, with D_s values falling in a region where radii of curvature are smaller (14.4 nm), which means that smoother surfaces are formed inside the cavities. Also, a decreasing trend of D_P, D_B, D_I and D_M was found with insertion of cobalt in the MoS_2 laminates (Table 4b–d), which is interpreted as enhancing the crystallite edge smoothing and surface density. This fundamental approach allowed to understand better the behavior of "CoMoS" phase type catalysts. Further work using a similar approach for "spent" MoS_2/Co and MoS_2 catalytic phases is underway for studying the role of carbon in the catalytic properties of those phases.

Experimental Methods

Catalyst Preparation. A black powder precipitate was synthesized by mixing 3 mmol of sodium molybdate ($Na_2MoO_4.2H_2O$) and 9 mmol of thioacetamide (CH_3CSNH_2) when dissolved in 30 mL of deionized water, and then 0.5 g of sodium silicate ($Na_2SiO_3.9H_2O$) was added into the solution under violent stirring. The pH value of the solution was adjusted to 6.0 by dropping 12 M hydrochloric acid (HCl) solution. 0.50 g of cobalt chloride ($CoCl_2$) was added to the solution before the hydrothermal reaction at a precise temperature, i.e., 220 °C [inside reactor chamber] for 4 h, thus allowing a natural cooldown. The catalyst was washed using a 1 M of Sodium Hydroxide (NaOH) to remove possible residues, mainly silicic acid and this was dried at 200 °C in autoclave. The synthesis follows the stoichiometry reaction: **1)** $6CoCl_26H_2O + 12Na_2MoO_4 + Na_2SiO_3 + 26HCl \rightarrow H_4SiCo_6Mo_{12}O_{40} + 26NaCl + 47H_2O + 6Cl_2$. **2)** $CH_3CSNH_2 + 2H_2O \rightarrow CH_3COOH + NH_{3+}H_2S$. **3)** $H_4SiCo_6Mo_{12}O_{40} + 27H_2S \rightarrow 12Co_{0.5}MoS_2 + H_2SiO_3 + 3H_2SO_4 + 25H_2O$ (for more information see Ramos *et al.*[18]).

Powder XRD and Rietveld refinement. All diffraction patterns were obtained with a Bruker Advance D-8 diffractometer fitted with Bragg-Brentano geometry, using CuKα radiation and a Lynxeye type detector. The intensities were obtained in the 2-theta ranges between 10 and 100° with a step of 0.019447° and a measuring time of 10 s per point. The crystalline structures were refined by Rietveld's method using TOPAS-Academic software[33]. All theoretical crystal density was calculated by the following equation: $\rho_{crystal} = (Z)(MM)(\text{Avogadro's number})^{-1}/\text{Cell volume}$; where Z is the number of molecules per cell and MM is the molecular weight. Radial Distribution: The distance (r) between atoms in MoS_2 and MoS_2(Co) crystallites was obtained by Radial Distribution Function G(r) up to 6.5 Å, in a Siemens D500 diffractometer fitted with a molybdenum anode X-ray tube. The intensities were measured in a step-by-step mode of 0.01°, from 2 to 110° (2θ), using the Radiale program[34].

Adsorption/Desorption isotherms. All the measurements of N_2 sorption isotherms were obtained at 76 K using a Quantachrome Autosorb 3B instrument under N_2 and He gases (UHP grade) conditions. Prior to isotherms runs, all the samples were outgassed for 12 h at 473 K. The specific surface areas were calculated from desorption isotherms using BET equation, while the pore structure parameters were determined by non-local density functional theory.

Experimental HRTEM microanalysis and Electron Tomography. Imaging of ultra-high resolution TEM was performed in an FEI Tecnai F20 instrument operating at 200 kV in STEM mode. Images were acquired every 2°, from −70 to + 70, totaling 71 images for each tilt series. The HRTEM images were collected in a JEOL ARM (200 F) instrument at operational voltage of 200 kV, which was fitted with a Cs corrector (CEOS GmbH) and FEG-STEM/TEM unit; a HAADF probe size was set to 0.095 nm with a current of 23.2 pA for bright field imaging, the condenser lens aperture size was set to 40 µm. A camera length (CL) of 8 cm/6 cm and collection angle of 68–280 mrad/90–270 mrad was set for STEM images, to eliminate contributions from un-scattered beams. The specimens were prepared for electron microscopy by crushing the powder between two glass slides, and rubbing a holey carbon grid across the crushed powder to capture the material. All images were reconstructed using Gatan Digital Micrograph® computational software and these were aligned with respect to each other using the center of mass of the particle[35]. These were reconstructed using total variation (TV) regularization, and visualized using the tomviz software[36].

Computational Software. Novawin 11.03 package was used for all the numerical simulations for porous size distribution and textural properties.

References

1. Chianelli, R. R., Berhault, G. & Torres, B. Unsupported transition metal sulfide catalysts: 100 years of science and application. *Catal. Today* **147**, 275–286 (2009).
2. Villareal, A. *et al*. Importance of the sulfidation step in the preparation of highly active NiMo/SiO2/Al2O3 hydrodesulfurization catalysts. *Catal. Today* **250**, 60–65 (2015).
3. Olivas, A., Alonso, G. & Fuentes, S. The catalytic activity of Ni/W bimetallic sulfide nanostructured catalysts in the hydrodesulfurization of dibenzothiophene. *Top. Catal.* **39**, 175–179 (2006).
4. Siadati, M. H., Alonso, G., Torres, B. & Chianelli, R. Open flow hot isostatic pressing assisted synthesis of unsupported MoS2 catalysts. *Appl. Catal. A* **305**, 160–168 (2006).
5. Stanislaus, A., Marafi, A. & Rana, M. S. Recent advances in the science and technology of ultra low sulfur diesel (ULSD) production. *Catal. Today* **153**, 1–68 (2010).
6. Morales-Ortuño, J. C., Ortega-Domínguez, R. A., Hernández-Hipólito, O., Bokhimi, X. & Klimova, T. E. HDS performance of NiMo catalysts supported on nanostructured materials containing titania. *Catal. Today* **271**, 127–139 (2016).
7. Gates, B. C. *et al*. Catalysts tor emerging energy applications. *MRS Bulletin* **33**, 429–435 (2008).
8. Farragher A.L. & Cossee P. Proceedings of the 5th International Congress on Catalysis, North-Holland, Amsterdam, 1301 (1973).
9. Hagenbach, G., Courty, P. & Delmon, B. Physicochemical investigations and catalytic activity measurements on crystallized molydbenum sulfide-cobalt sulfide mixed catalysts. *J.Catal.* **31**, 264–273 (1973).
10. Candia R. *et al*. Proceedings of the 8th International Congress on Catalysis, Dechema, Frankfurt-an-Main, **2**, 375 (1984).
11. Daage, M. M. & Chianelli, R. R. Structure-Function Relations in Molybdenum Sulfide Catalysts: The "Rim-Edge" Model. *J. Cat.* **149**, 414–427 (1994).
12. Perdew, J. P., Burke, K. & Ernzerhof, M. Generalized Gradient Approximation Made Simple. *Phys. Rev. Lett.* **77**, 3865 (1996).
13. Hammer, B., Hansen, L. B. & Nørskov., K. Improved adsorption energetics within density-functional theory using revised Perdew-Burke-Ernzerhof functionals. *Phys. Rev. B* **59**, 7413 (1999).
14. Lauritsen, J. V. *et al*. Location and coordination of promoter atoms in Co- and Ni-promoted MoS2-based hydrotreating catalysts. *J. Catal.* **249**, 220–233 (2007).
15. Remškar, M., Viršek, M. & Mrzel, A. The MoS2 nanotube hybrids. *Appl. Phys. Lett.* **95**, 133122 (2009).
16. Camacho-Bragado, G. A., Elechiguerra, J. L. & Yacaman, M. Characterization of low dimensional molybdenum sulfide nanostructures. *J. Mat. Char.* **59**, 204–212 (2008).
17. Blanco, E., Afanasiev, P., Berhault, G., Uzio, D. & Loridant, S. Resonance Raman spectroscopy as a probe of the crystallite size of MoS2 nanoparticles. *Comp. Rendus Chimie* **19**, 1310–1314 (2016).
18. Ramos, M. A. *et al*. Spherical MoS2 micro particles and their surface dispersion due to addition of cobalt promoters. *Rev. Mex. Fís.* **57**, 220–223 (2011).
19. Ramos, M. A., Berhault, G., Ferrer, D. A., Torres, B. & Chianelli, R. R. HRTEM and molecular modeling of the MoS2–Co9S8 interface: understanding the promotion effect in bulk HDS catalysts. *Catal. Sci. Technol.* **2**, 164–178 (2012).
20. Ramos, M. *et al*. *In-situ* HRTEM study of the reactive carbide phase of Co/MoS2 catalyst. *Ultramicroscopy* **127**, 64–69 (2013).
21. Casillas, G. *et al*. Elasticity of MoS2 Sheets by Mechanical Deformation Observed by *in Situ* Electron Microscopy. *J. Phys. Chem. C* **119**, 710–715 (2015).
22. Hansen, L. P., Johnson, E., Brorson, M. & Helveg, S. Growth Mechanism for Single- and Multi-Layer MoS2 Nanocrystals. *J. Phys. Chem. C* **118**, 22768–22773 (2014).
23. Midgley, P. A. & Dunin-Borkowski, R. E. Electron tomography and holography in materials science. *Nature Mater.* **8**, 271–280 (2009).
24. Muller, D. A. Structure and bonding at the atomic scale by scanning transmission electron microscopy. *Nature Mater.* **8**, 263–270 (2009).
25. Ziese, U., de Jong, K. P. & Koster, A. J. Electron tomography: a tool for 3D structural probing of heterogeneous catalysts at the nanometer scale. *Applied Catalysis A: General* **260**, 71–74 (2004).
26. Arslan, I., Marquis, E. A., Homer, M., Hekmaty, M. A. & Bartelt, N. C. Towards better 3-D reconstructions by combining electron tomography and atom-probe tomography. *Ultramicroscopy* **108**, 1579–1585 (2008).
27. Niemantsverdriet J.W. *et al*. in Catalysis – Biocatalytic Processes Encyclopedia of Life Support Systems (EOLSS) (2007).
28. Somorjai G.A. Introduction to Surface Chemistry and Catalysis (ed. Wiley) (New York, 1994).
29. Ertl, G. Oscillatory Catalytic Reactions at Single-Crystal Surfaces. *Adv. Catal.* **37**, 213–277 (1990).
30. Imbihl, R. & Ertl, G. Oscillatory Kinetics in Heterogeneous Catalysis. *Chem. Rev.* **95**, 697–733 (1995).
31. Wang, S. *et al*. A New Molybdenum Nitride Catalyst with Rhombohedral MoS2 Structure for Hydrogenation Applications. *J. Am. Chem. Soc.* **137**, 4815–4822 (2015).
32. Galindo-Hernández, F., Domínguez, J. M. & Portales, B. Structural and textural properties of Fe2O3/γ-Al2O3 catalysts and their importance in the catalytic reforming of CH4 with H2S for hydrogen production. *J. Power Sources* **287**, 13–24 (2015).

33. Coelho A. TOPAS-academic V4.1, Coelho Software, Brisbane, Australia (2007).
34. Magini, M. *et al*. Programme en FORTRAN IV pour l'analyse des données expérimentales relatives à la diffusion des rayons X par des substances liquides, amorphes et microcristallisées. *J. Appl. Cryst.* **5**, 14 (1972).
35. Sanders, T., Prange, M., Akatay, C. & Binev, P. Physically motivated global alignment method for electron tomography. *Adv. Struct. Chem. Imaging.* **1**, 11–11 (2015).
36. Sanders, T. Discrete Iterative Partial Segmentation Technique (DIPS) for Tomographic Reconstruction. *IEEE Trans. Comp. Imag.* **2**, 71–82 (2016).

Acknowledgements

This project was funded by Mexican Science Council [CONACyT-México] and Energy Ministry [Sener] under solicitation grant #177077 (IMP project Y.61006). Instituto Mexicano del Petróleo for usage of laboratory equipment and facilities. I.A. was supported by the Laboratory Directed Research and Development Program at the Pacific Northwest National Laboratory. To the Universidad Autónoma de Ciudad Juárez for economical support in article processing by grant #SEP-23-007-B of Programa para el Desarrollo Profesional Docente para el tipo superior (PRODEP).

Author Contributions

M. Ramos was in charge of chemical synthesis and scanning electron imaging. F. Galindo-Hernández completed all computer assisted numerical simulations. I. Arslan and T. Sanders performed electron tomography measurements and computer assisted reconstruction. J.M. Domínguez is the principal investigator on this particular Energy project in charge of design and supervision of all experiments. This manuscript was mainly typed by M. Ramos, F. Galindo, I. Arlsan and J.M. Domínguez.

Additional Information

Supplementary information accompanies this paper at https://doi.org/10.1038/s41598-017-12029-8.

Competing Interests: The authors declare that they have no competing interests.

Publisher's note: Springer Nature remains neutral with regard to jurisdictional claims in published maps and institutional affiliations.